Bulletin of the Seismological Society of America, Vol. 106, No. 6, pp. 2459–2468, December 2016, doi: 10.1785/0120160091

Real-Time Moment Magnitude and Stress Drop with Implications for Real-Time Shaking Prediction

by Alon Ziv and Itzhak Lior

Abstract Despite the potentially dramatic effect of the stress drop on ground-motion intensity, currently available earthquake early warning systems that deliver peak ground-motion predictions do not account for the effect of this parameter. To address this issue, a new evolutionary algorithm for determining stress drop and moment magnitude in real time is described. It consists of two distinct modules: one processes data recorded by individual stations and another computes event-average stress drops and moment magnitudes. To speed up the analysis, the real-time algorithm deviates from standard procedures of stress-drop determination in several ways. Because these time-saving measures come at the price of accuracy, a quality-control parameter is introduced, which quantifies the discrepancy between the observed and modeled ground motion.

The results of implementing the algorithm offline using KiK-borehole data from Japan are presented. It is shown that it is possible to recover the moment magnitudes and the stress drops in real time. Two example timelines of seismic moment and stress drop are presented. These show that the source parameters of small-to-moderate earthquakes may be estimated quite accurately within 5 to 10 s since the first trigger, whereas those of larger magnitudes (i.e., $M_w > 6$) take 20–30 s. Finally, ground-motion prediction equations for the velocity's root mean square and peak ground velocity are presented. Once the epicenter, seismic moment, and stress drop are determined using a few stations nearest to the epicenter, their values can be input into those equations to get the ground-motion intensity at sites further away from it.

Introduction

Together with the hypocentral distance and the seismic moment, the stress drop is among the three most important source parameters affecting ground-motion intensity (Hanks, 1979; Hanks and McGuire, 1981; Baltay and Hanks, 2014; Lior *et al.*, 2016). Nevertheless, currently available earthquake early warning systems (EEWS), delivering peak ground-motion predictions (e.g., Böse *et al.*, 2007; Cua *et al.*, 2009; Zollo *et al.*, 2009; Brown *et al.*, 2011; Satriano *et al.*, 2011), do not account for the effect of the stress drop on the ground-motion intensity. It is thus important to develop a real-time algorithm for stress-drop determination.

Stress drop, the driving force behind the rupture process, may be expressed as

$$\Delta\tau = \frac{7}{16} M_0 \left(\frac{f_0}{kC_S}\right)^3 \tag{1}$$

(Hanks and Thatcher, 1972), with M_0, f_0, and C_S being the seismic moment, the corner frequency, and the shear wave-speed, respectively, and k is a constant (Brune, 1970; Madariaga, 1976). The inference of seismic moment and corner frequency entails transforming the ground-motion time series into the spectral domain, and fitting the displacement spectra Ω with the omega-square model:

$$\Omega(f) = \frac{\Omega_0}{1 + (\frac{f}{f_0})^2} \tag{2}$$

(Aki, 1967; Brune, 1970), in which Ω_0 is the low-frequency spectral plateau, which is related to the seismic moment and the hypocentral distance as

$$\Omega_0 = \frac{M_0 \mathrm{rpFS}}{4\pi\rho C^3 R}, \tag{3}$$

in which rp is the radiation pattern, FS is a free-surface correction factor, C is the body-wave velocity at the source (P or S, depending on the spectra), R is the hypocentral distance, and ρ is the density. Thus, the hypocentral distance is needed for stress-drop determination, and thanks to recent advances in real-time P- and S-phase picking (e.g., Küperkoch *et al.*, 2012; Kurzon *et al.*, 2014; Ross and Ben-Zion, 2014), its determination in real time is quite robust. Use of equation (2) is appropriate only in cases where the permanent

ground displacement is much smaller than the amplitude of the transient motion. To a large extent, the popularity of this far-field model stems from the fact that the vast majority of seismic observations do satisfy this criterion. Because here, however, stations nearest to the epicenter are used, the risk of not meeting the far-field criterion is indismissible, and it is important to check for model consistency. This issue is addressed in the Data Quality Control and Model Consistency Check section.

This article is organized as follows: first, an evolutionary algorithm for determining the seismic moment and stress drop in real time is described. Then, the results of implementing this algorithm offline using KiK-borehole data from Japan are presented. A couple of example timelines of seismic moment and stress drop are shown, which illustrate the performances of the proposed scheme. Finally, the potential of real-time seismic moment and stress drop for real-time ground-motion prediction is discussed.

Real-Time Evolutionary Algorithm

Main Deviations from Standard Procedures of Stress-Drop Determination

To speed up the analysis, the real-time algorithm deviates from standard procedures of stress-drop determination in several ways. In contrast to standard procedures of high-pass filtering strong-motion records to reduce distortions caused by tilts and permanent offsets, here the analyses are performed on unfiltered seismograms. The benefit of avoiding high-pass filtering of the data is twofold: it cuts down the computation time, and it prevents the removal of the low-frequency signals that dominate large earthquakes. Because the constant trend resulting from single integration of tilted accelerograms is much smaller than that caused by double integration, in this study the spectral attributes Ω_0 and f_0 are solved for by fitting the velocity spectra $\dot{\Omega}$ with the corresponding omega-square model:

$$\dot{\Omega}(f) = 2\pi f \frac{\Omega_0}{1 + (\frac{f}{f_0})^2}. \tag{4}$$

Use of equation (4) instead of equation (2) reduces the harmful effects that tilts and permanent offsets may have on the stress-drop assessment, and makes high-pass filtering the accelerograms more dispensable.

Although the standard approach for stress-drop determination of local earthquakes is to use fixed data intervals of *P* or *S* waves, the real-time scheme introduced here uses incrementally increased data intervals, starting at the time of the first *P*-wave arrivals. The obvious advantage of this evolutionary approach is that initial assessment becomes available sooner than it would have been had the standard approach been implemented. A consequence of this approach is that *P* and *S* phases very quickly get mixed up. This issue is addressed later.

Finally, the effects of anelastic dissipation and near-surface attenuation, which are accounted for by standard procedures, are neglected here. Previous studies show that anelasticity is not important at distances less than about 60 km (Wu *et al.*, 2005; Wu and Zhao, 2006; Lior *et al.*, 2016), and near-site effects mainly attenuate frequencies that are well above the corner frequencies of $M_w > 4$ (Oth, Parolai, *et al.*, 2011; Baltay and Hanks, 2014). Because distances greater than 60 km and $M_w < 4$ are irrelevant for EEWS, neglecting these effects is justified.

In summary, the analysis is expedited by using unfiltered data, by implementing an evolutionary scheme with data intervals starting at the time of the first *P*-wave arrivals, and by not accounting for anelastic and near-site attenuations. These time-saving measures come at the price of accuracy, and it is necessary to compensate for them by passing the data through a strict quality control.

Data Quality Control and Model Consistency Check

The far-field spectra of body waves depend on the azimuth at which these waves leave the source (Madariaga, 1976). This azimuthal dependency introduces within-event variability in the corner frequencies. Because the stress drop is a function of the corner frequency cubed (equation 1), the within-event variability in the corner frequencies is mapped into a much greater variability in the stress-drop estimates. An additional consequence of the strong stress-drop dependency on the corner frequency is that small errors in the corner-frequency estimates may cause large errors in the stress-drop estimates (Cotton *et al.*, 2013). Furthermore, use of the omega-square model is appropriate only in the far field, where the permanent ground displacement is much smaller than the amplitude of the transient displacement. Finally, the inference of the stress drop is model based (e.g., Brune, 1970), and these models do not account for various rupture propagation effects, such as directivity and segmentation. Thus, large discrepancies between modeled and observed spectra may arise when the source process defies the simplifying assumptions underlying these models. Therefore, whether in real time or not, estimating stress drops is a challenging task, and unless a statistically meaningful number of good-quality seismic records with good azimuthal coverage are available, determining the stress drop may not be robust. To address the robustness issue, data quality assessments and model consistency checks are critical for real-time stress-drop determination.

To assess the data quality and check for model consistency, a parameter that quantifies the discrepancy between the observed and modeled ground motion is introduced. By inserting the omega-square relation into the Parseval's theorem, Lior *et al.* (2016) obtained the following expression for the root mean square (rms) velocity:

$$v_{\mathrm{rms}} = 2\pi\Omega_0 \sqrt{\frac{\pi}{2}\frac{f_0^3}{\Delta T}}, \tag{5}$$

in which ΔT is the data interval. A discrepancy parameter that quantifies the disagreement between observed and predicted ground velocities is

$$\text{discrepancy} = \left| \log\left(v_{\text{rms}} / 2\pi\Omega_0 \sqrt{\frac{\pi}{2}\frac{f_0^3}{\Delta T}} \right) \right|. \qquad (6)$$

Results whose discrepancy parameter exceeds some prespecified value are disregarded. Next, an algorithm for determining the moment magnitude and the stress drops in real time is described.

Detailed Description

The algorithm described here may either be integrated into existing EEWS or form the basis for a totally new one. It consists of two distinct modules. The first is an individual station analyst (ISA), which processes data recorded by individual stations. The second module is a multistation aggregator (MSA), which performs a quality check on the ISA outputs and computes event-average stress drops and M_w.

An ISA proceeds along the following steps:

1. Run a *P*- and *S*-phase picker (e.g., Kurzon *et al.*, 2014; Ross and Ben-Zion, 2014) and proceed to the next step after *S* picking.
2. Initialization:
   2.1. estimate a hypocentral distance according to: $R = \Delta T_{S-P}(\text{s}) \times 8(\text{km/s})$, with ΔT_{S-P} being the interval between the *P* and *S* arrivals;
   2.2. extract a data interval, starting at the time of the first *P*-wave arrival, according to $\Delta T = \max(\Delta T_{S-P}, 5\text{ s})$.
3. Data preparation:
   3.1. integrate accelerograms to get a velocity time series;
   3.2. apply a zero-offset correction; and
   3.3. obtain velocity rms for the entire data interval.
4. Spectral inversion:
   4.1. apply a Hann window;
   4.2. obtain velocity spectra;
   4.3. downsample the spectra at constant intervals of log-of-frequency;
   4.4. employ equation (4) to infer Ω_0 and f_0 via a 2D grid search.
5. Output:
   5.1. employ equation (3) to get M_0;
   5.2. employ equation (1) to get $\Delta\tau$;
   5.3. use the moment–magnitude relation of Hanks and Kanamori (1979) to get M_w;
   5.4. output the following parameters: R, v_{rms}, Ω_0, f_0, M_w, and $\Delta\tau$.
6. Exit criteria check:
   6.1. exit if the total data interval reached 60 s;
   6.2. exit if the rms of the next data packet falls below 100 times the presignal rms.
7. Append the new data packet to the previous data interval and return to step 3.

The MSA module, which computes event-average M_w and $\Delta\tau$, is activated by the first ISA output. It reports event-average parameters each time a new ISA result becomes available. The MSA employs equation (4) to get a discrepancy parameter and excludes results whose discrepancy parameter exceeds some prespecified value.

Explanatory notes and comments are as follows:

- The only notable time-consuming computation in the above algorithm is the Fourier transformation in step 4.2 of the ISA. Calculating the velocity spectra of one component instead of three saves time. In that case, to approximately make up for the missing spectra, the Ω_0 in equation (3) should be replaced by the Ω_0 corresponding to that component multiplied by $\sqrt{3}$.
- The downsampling in step 4.3 is necessary to avoid overweighting the highest frequencies when fitting the spectra to Brune's omega-square model (Allmann and Shearer, 2009). In addition, it has the advantage of reducing the computation time of the grid search.
- In this study, the following parameter settings are used: $k = 0.37$, $C_P = 5800$ m/s, $C_S = 3200$ m/s, $\text{rp}_P = 0.52$, $\text{rp}_S = 0.63$, FS = 2, and $\rho = 2600$ kg/m^3, with the subscripts *P* and *S* signifying the seismic phase.
- The data intervals are set such that *P* and *S* phases get mixed up. For that reason, rp/C^3 in equation (3) is replaced by the weighted average $X_P \text{rp}_P/C_P^3 + (1 - X_P)\text{rp}_S/C_S^3$, in which X_P is the fraction of *P* waves.

Previously proposed algorithms for real-time M_w and stress-drop determination differ markedly from the one described above. Colombelli and Zollo (2015) examine multistation averaged time series of the logarithm of the distance-corrected peak displacement and show that the time and the amplitude of the displacement plateau may be used to assess the magnitude and the rupture length. Once these source parameters become available, estimating the stress drop is straightforward. Although Caprio *et al.* (2011) does not explicitly propose an algorithm for stress-drop determination, their evolutionary algorithm and the one described here share some features; both schemes are evolutionary, employ the omega-square model, obtain M_w through spectral inversion, and rely on getting a robust epicentral distance from a different algorithm. The main differences between the two is that (1) there the quality factor is solved for together with f_0 and Ω_0, whereas here only the last two parameters are solved for; (2) there the data are band-pass filtered, whereas here they are not; (3) there the displacement spectra are modeled, whereas here the velocity spectra are used; and (4) there the three ground-motion components are Fourier transformed, whereas here only the vertical component is Fourier transformed.

Application to Japan Earthquakes

Comparison between surface and borehole acceleration records from Japan reveals that the former are much more strongly affected by site amplification and near-site attenuation than the latter (e.g., Oth, Parolai, *et al.*, 2011; Oth, Bindi, *et al.*, 2011). Because the source spectra of small-

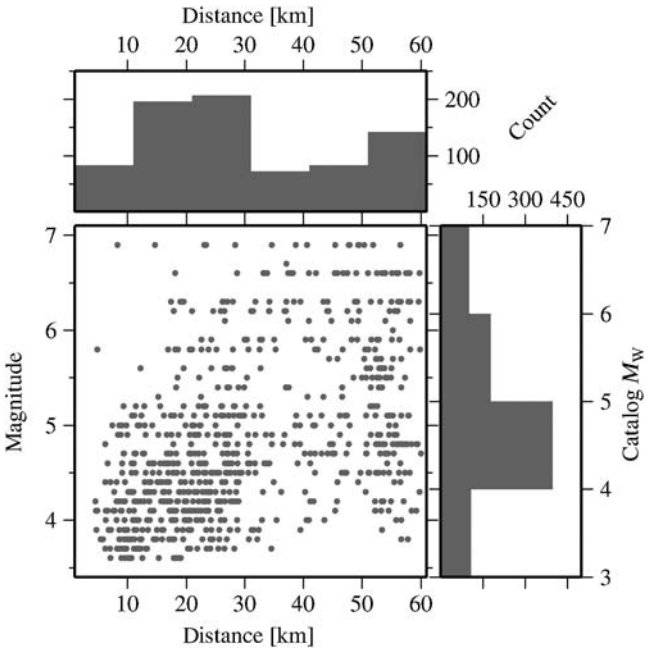

Figure 1. Waveform distribution according to catalog M_w and hypocentral distances. A total of 587 seismograms, which correspond to 347 earthquakes, were used in this study.

to-moderate earthquakes are difficult to extract from records that are strongly distorted by such effects, use of borehole data for testing the newly proposed algorithm is preferable. In future implementations, in places where borehole records are unavailable, it would be sensible to exclude stations located on soft sediments and correct the spectra using predetermined near-site attenuation coefficients.

Data

The data set consists of 587 accelerograms recorded by Japan's KiK-net borehole accelerometers, with hypocentral distances of up to 60 km (Fig. 1). These records are associated with 347 earthquakes that occurred between 2000 and 2014. F-net revised M_w (hereafter, catalog M_w) and hypocenters are used. Details regarding the five largest earthquakes are provided in Table 1. Only vertical components are used in this study. Although in real-time implementation the *P* and *S* phases are to be picked automatically, here they were picked semimanually, and the T_{S-P} intervals were set to 1 s per 8 km of the hypocentral distance reported in the F-net catalog.

Single-Station Stress Drop and Moment Magnitude Estimates

The data were processed offline using the real-time algorithm described in the Detailed Description section. Results shown here correspond to the closing outputs of the ISA module, that is, the last f_0, Ω_0, M_w, and $\Delta\tau$ estimates inferred from individual stations. The average closing data interval equals 27 s (Fig. 2a). It increases with magnitude

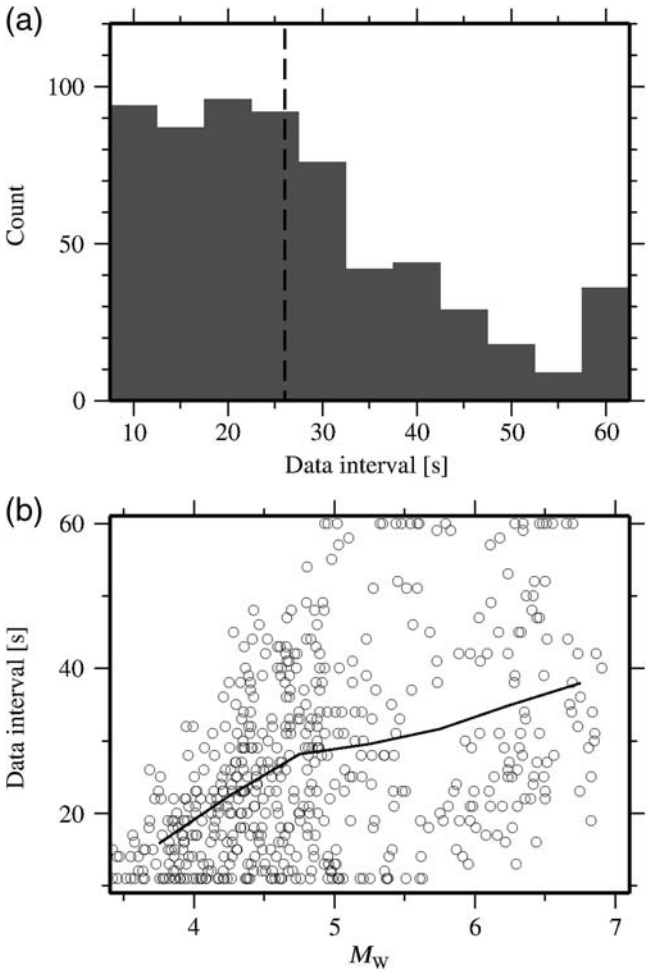

Figure 2. Data interval distribution. (a) A histogram of the data intervals, with a vertical dashed line indicating the average data interval. (b) Data interval as a function of M_w. The solid line indicates a moving average.

from about 15 s for the smallest earthquakes in the data set to nearly 40 s for the largest ones (Fig. 2b).

Example spectra of records whose discrepancy parameter is well below and well above 0.5 are presented in Figure 3a and 3b, respectively. It is clear from these examples that records with a large discrepancy parameter cannot

Table 1
List of Five Largest Earthquakes with M_w and Locations as Reported by the F-net Catalog

Date (yyyy/mm/dd)	M_w	Name	Epicenter	
			Longitude (°)	Latitude (°)
2000/10/06	6.6	Tottori	35.28	113.34
2004/10/23	6.6	Chūestsu	37.29	138.86
2005/03/20	6.6	Fukuoka	33.73	130.17
2007/07/16	6.6	Chūestsu offshore	37.55	138.60
2008/06/14	6.9	Iwate–Miyagi	39.03	140.88

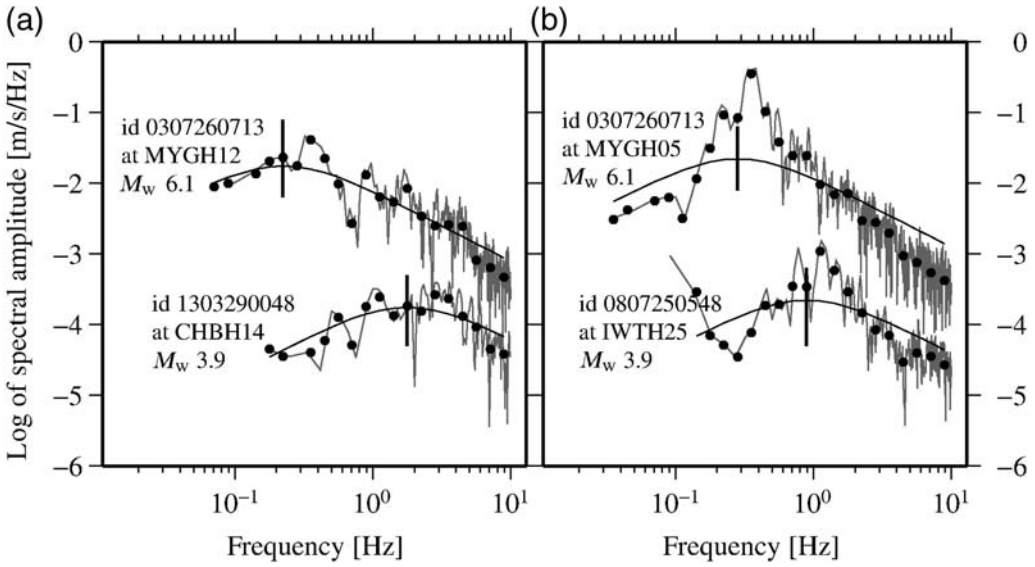

Figure 3. Example spectra. (a) Spectra of records whose discrepancy parameter is much less than 0.5. (b) Spectra of records whose discrepancy parameter is greater than 0.5. Observed and modeled spectra are indicated by gray and black curves, respectively. The spectra are resampled at equal log-of-frequency spacing (black dots). Vertical bars indicate the corner frequencies. Event IDs, station names, and catalog M_w are indicated next to each example.

resolve the source parameters. Indeed, visual examination of the time-integrated accelerograms (not shown) corresponding to a discrepancy parameter greater than 0.5 reveals that most of them are strongly distorted by tilt and/or permanent offset. A smaller fraction of these records do not show signs for such distorting effects and are simply incompatible with the omega-square model. Furthermore, a plot of observed versus theoretical v_{rms} calculated using equation (5) reveals a fairly good agreement between theory and observations for data points whose discrepancy parameter is smaller than 0.5 (Fig. 4). Thus, here, results whose discrepancy parameter exceeds 0.5 are treated as outliers. As the fraction of these records is about 10% (inset of Fig. 4), disregarding them does not result in a severe data loss.

The reciprocal of the corner frequency $1/f_0$ and the distance-corrected spectral plateau $\Omega_0 R$ as a function of the catalog magnitude are shown in Figure 5, with circles and crosses indicating results whose discrepancy parameter is smaller than or greater than 0.5, respectively. Both $1/f_0$ and $\Omega_0 R$ associated with small discrepancy parameters are strongly correlated with the catalog M_w. In contrast, many of the data points associated with large discrepancy parameters plot outside the main cluster and are clearly uncorrelated with the catalog M_w. Thus, the discrepancy parameter is an effective tool for real-time quality control and model consistency checks.

The reciprocal of the corner frequency as a function of the real-time M_w is shown in Figure 6a, along with lines of constant stress drop (dashed lines) and a best-fitting curve (solid line) as follows: $\log_{10}(1/f_0) = -2.04 + 0.45M_w$, with correlation coefficient and standard deviation of 0.9 and 0.15 (in $\log_{10}$ units), respectively. That the inclination of the line

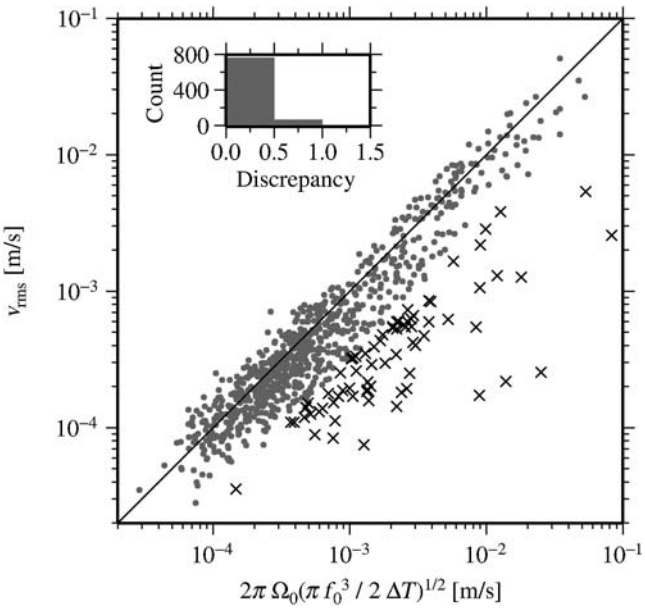

Figure 4. Observed versus theoretical v_{rms} (i.e., right side of equation 5). Gray circles and black crosses indicate results whose discrepancy parameter is lesser or greater than 0.5. Record count as a function of the discrepancy parameter is shown at the top-left corner. The percentage of greater than 0.5 discrepancy parameters equals 11%.

of best-fitting curve is less steep than those of the constant stress drop indicates larger stress drop for larger magnitudes. Individual stress-drop estimates span two orders of magnitudes, with an average value of about 4 MPa (Fig. 6b). This result is in agreement with Oth (2013), who used standard procedure for stress-drop calculation of Japanese earthquakes.

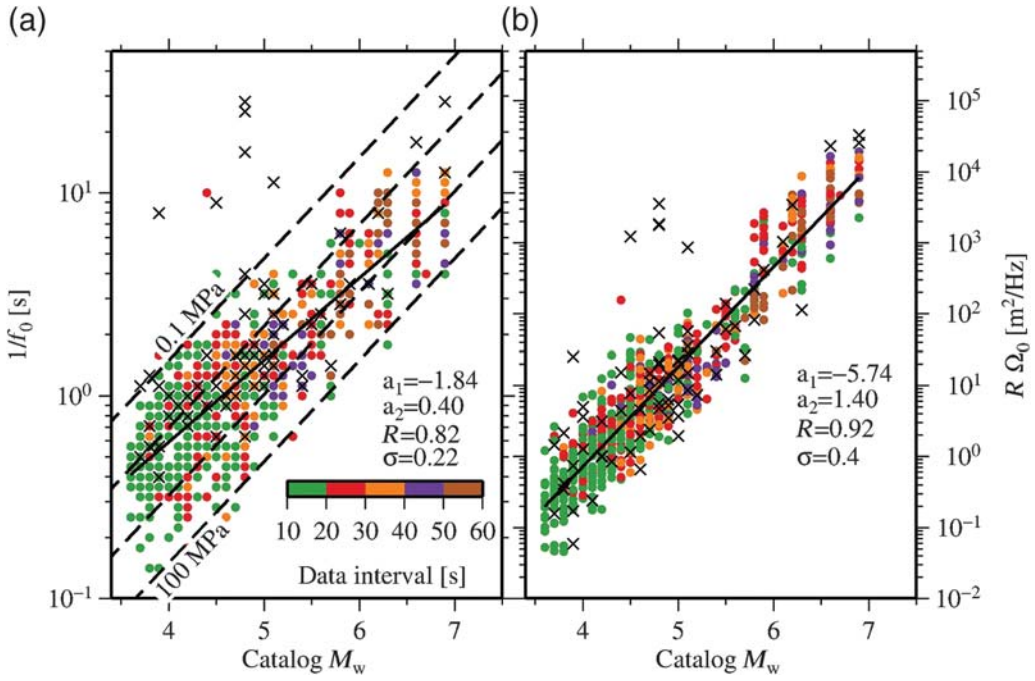

Figure 5. The spectral parameters as a function of the catalog M_w. (a) The reciprocal of the corner frequency $1/f_0$ as a function of the catalog M_w. Dashed lines indicate constant stress drops of 0.1, 1, 10, and 100 MPa, and the solid line indicates the linear regression fit to $\log(1/f_0)$ versus M_w. (b) The distance-corrected spectral plateau $\Omega_0 R$ as a function of the catalog M_w. Circles and crosses indicate discrepancy parameters lesser than or greater than 0.5, respectively, and the color code indicates the closing data interval.

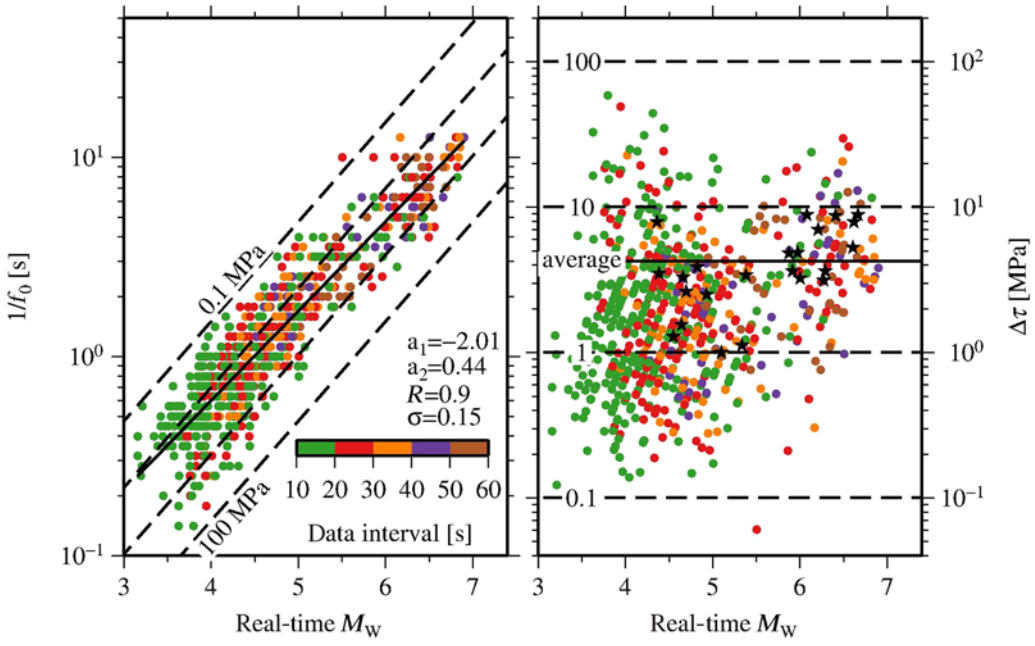

Figure 6. A summary diagram of the closing results, that is, the last outputs of the individual station analyst (ISA) module. (a) The reciprocal of the corner frequency $1/f_0$ as a function of M_w. Dashed lines indicate constant stress drops of 0.1, 1, 10, and 100 MPa, and the solid line indicates the linear regression fit to $\log(1/f_0)$ versus M_w. (b) The stress drop as a function of M_w. The solid horizontal line indicates the average stress drop; black stars indicate event-average values; and the color code indicates the closing data interval.

Of the 347 earthquakes analyzed in this study, 23 were recorded by more than three stations (and 63 were recorded by more than two). Event-average stress drops of these well-recorded earthquakes span only one order of magnitude, between 1 and 10 MPa (black stars in Fig. 6b). Nevertheless, the tendency for larger earthquakes to have larger stress drops is still apparent for this subset of the data. Comparison between real-time and catalog M_w reveals excellent agreement

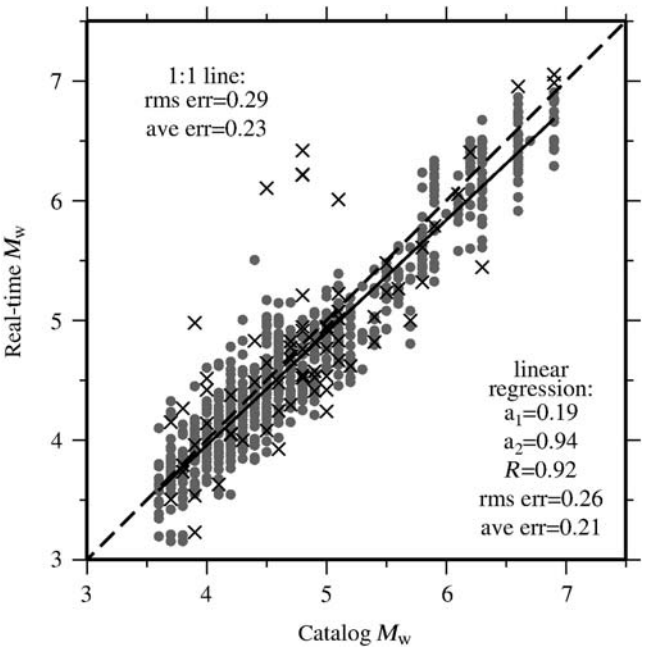

Figure 7. The M_w obtained in this study as a function of the catalog M_w. Gray circles and black crosses indicate results whose discrepancy parameters are lesser and greater than 0.5, respectively. The solid line is a best-fitting curve to real-time $M_w = a_1 + a_2$ catalog M_w, with the fitting coefficients (a_1 and a_2), the correlation coefficient (R), the root mean square (rms), and the average M_w discrepancies reported at the bottom-right corner. The rms and the average M_w discrepancies with respect to the 1:1 line (dashed line) are reported at the top-left corner.

between the two (Fig. 7). Linear regression yields real-time $M_w = 0.19 + 0.94$ catalog M_w, with correlation coefficient and an average M_w discrepancy that are equal to 0.92 and 0.21, respectively.

Example Multistation Timelines

Representative multistation timelines of stress-drop and M_w estimates are shown in Figure 8 for two earthquakes, with thin gray lines corresponding to individual station estimates, and thick black lines indicating the multistation average. The source parameters of small-to-moderate earthquakes may be estimated quite accurately within 5 to 10 s since the first trigger (Fig. 8c,d). For larger magnitudes, that is, $M_w > 6$, the assessment of these parameters takes longer. In particular, the M_w estimates of such earthquakes rise with time after the first trigger and stabilize only after 20–30 s (Fig. 8a,b). The exceptionally large within-event stress drop and M_w variability of M_w 6.2 (Fig. 8a,b) may be due to directivity and other rupture propagation effects.

Implications for Ground-Motion Prediction

Substituting equations (1) and (3) into equation (5) yields a ground-motion prediction equation (GMPE) for v_{rms} in terms of the hypocentral distance, the seismic moment, and the stress drop:

$$v_{rms} = \left[\frac{\text{rpFS}}{2\rho C^3}\sqrt{\frac{\pi}{2}(kC_S)^3\frac{16}{7}}\right]\left(\frac{1}{R}\sqrt{\frac{\Delta\tau M_0}{\Delta T}}\right), \quad (7)$$

in which the term inside the square brackets collects all the medium and site-specific constants, and the term inside the round brackets contains the source parameters and the data interval. Because the value of the stress-drop spans two orders of magnitude, it may have a dramatic effect on the ground-motion intensity, and earthquakes releasing similar seismic moments may give rise to radically different ground-motion amplitudes if their stress drops differ notably.

Plots of v_{rms} as a function of the term inside the round brackets of equation (7) are shown, once with the stress drop replaced by the average stress drop of the entire population (Fig. 9a) and once with the stress drop being the earthquake-specific stress drop (Fig. 9b). In either case, the slope of the least-square fit is close to −1, thus validating the scaling of the above expression. Although in Figure 9a large stress drops plot above small ones, in Figure 9b different stress-drop values plot on top of each other. The switch from a population average stress drop to earthquake-specific stress drops reduces the rms error by 30%, from 0.22 to 0.16 (in $\log_{10}$ units), and reduces the average error (also in $\log_{10}$ units) from 0.18 to 0.14.

Linear regression of log(PGV) versus $\log(v_{rms})$ yields $\log(\text{PGV}) = 0.3 + 0.87\log(v_{rms})$ with correlation coefficient of 0.9 (Fig. 10). Consequence of the close-to-linear relation between peak ground velocity (PGV) and v_{rms} is that PGV and the term inside the round brackets of equation (7) are also strongly correlated (Fig. 10). The following relation is obtained: $\log(\text{PGV}) = -9.82 - 0.8R[\Delta T/(M_0\Delta\tau)]^{1/2}$, with correlation coefficient and average error (in $\log_{10}$ units) equal to −0.75 and 0.18, respectively. Thus, once the epicenter, the seismic moment, and the stress drop are determined using a few stations nearest to the epicenter, their values can be plugged into the linear regression lines in Figures 9b and 10 to assess the ground-motion intensity at sites further away from it.

Summary

A new real-time evolutionary algorithm for stress drop and M_w is described. It consists of two distinct modules: one processes data recorded by individual stations and another computes event-average stress drops and M_w. To speed up the analysis, the real-time algorithm deviates from standard procedures of stress-drop determination using unfiltered data by implementing an evolutionary scheme with data intervals starting at the time of the first *P*-wave arrivals, and by not accounting for the anelastic and near-site attenuations. To make up for these time-saving measures, a quality-control parameter is introduced that quantifies the discrepancy between the observed and modeled ground motion. Results whose quality-control parameter exceeds some prespecified value are disregarded.

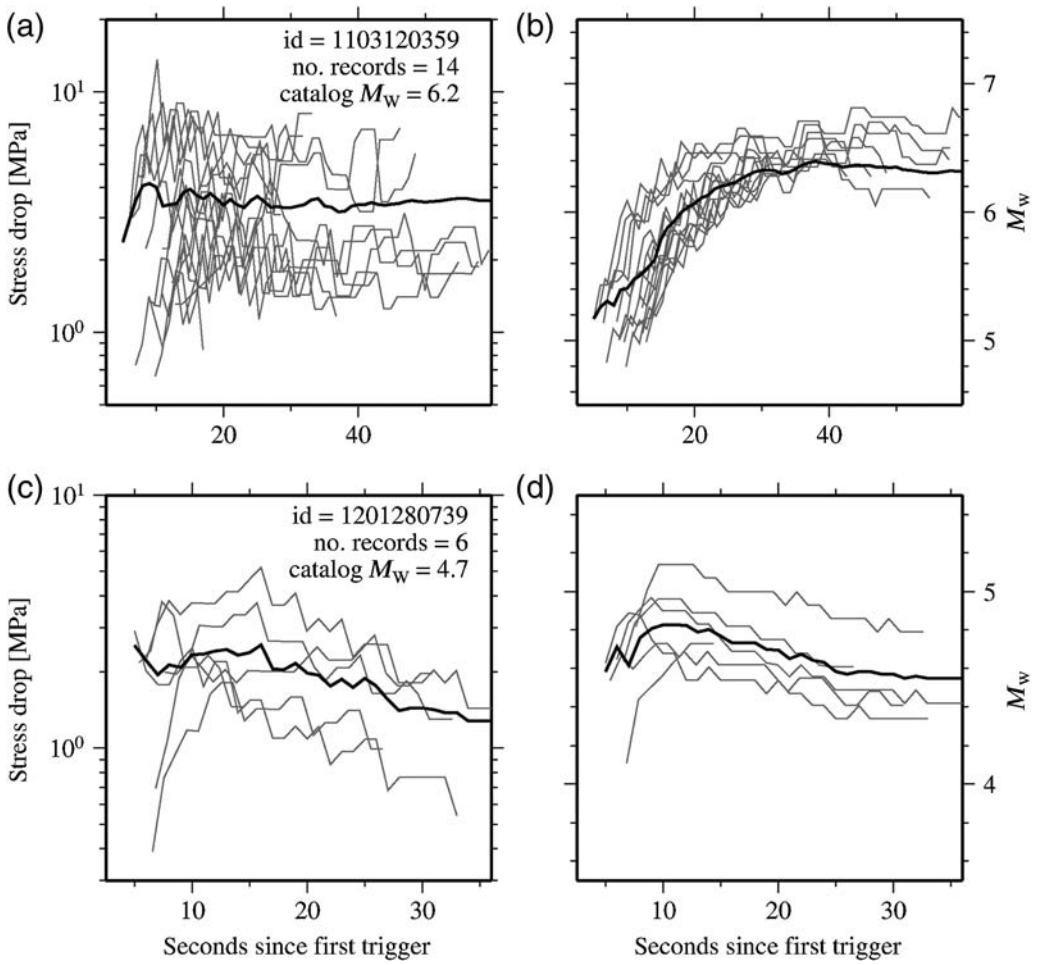

Figure 8. Example timelines of two representative earthquakes. (a) Stress drop as a function of time since the first trigger for M_w 6.2. (b) M_w as a function of time since the first trigger for M_w 6.2. (c) Stress drop as a function of time since the first trigger for M_w 4.7. (d) M_w as a function of time since the first trigger for M_w 4.7. Thin gray lines indicate results of individual stations and thick black curves indicate event-averaged values.

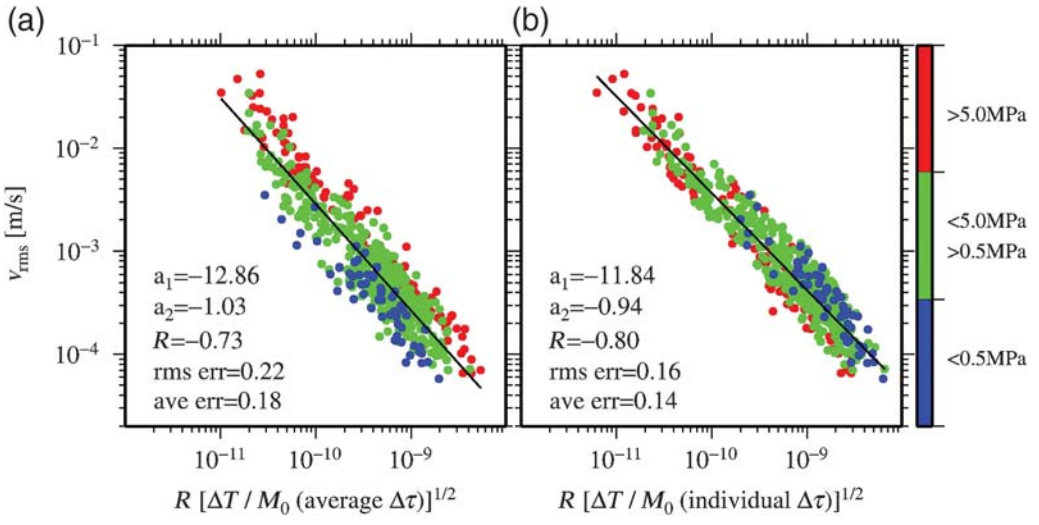

Figure 9. Observed v_{rms} as a function of calculated $R(\Delta T/\Delta\tau M_0)^{0.5}$. (a) The $\Delta\tau$ is replaced by the average stress drop of the population. (b) The $\Delta\tau$ is set to be equal to the earthquake-specific stress drop, that is, the closing outputs of the ISA module. Solid lines are best-fitting curves to $\log(v_{rms}) = a_1 + a_2 \log[R(\Delta T/\Delta\tau M_0)^{0.5}]$. The fitting coefficients (a_1 and a_2), the correlation coefficients (R), and the rms of the discrepancy between predicted and observed velocities are reported on each panel. The color code is indicative of the stress drop.

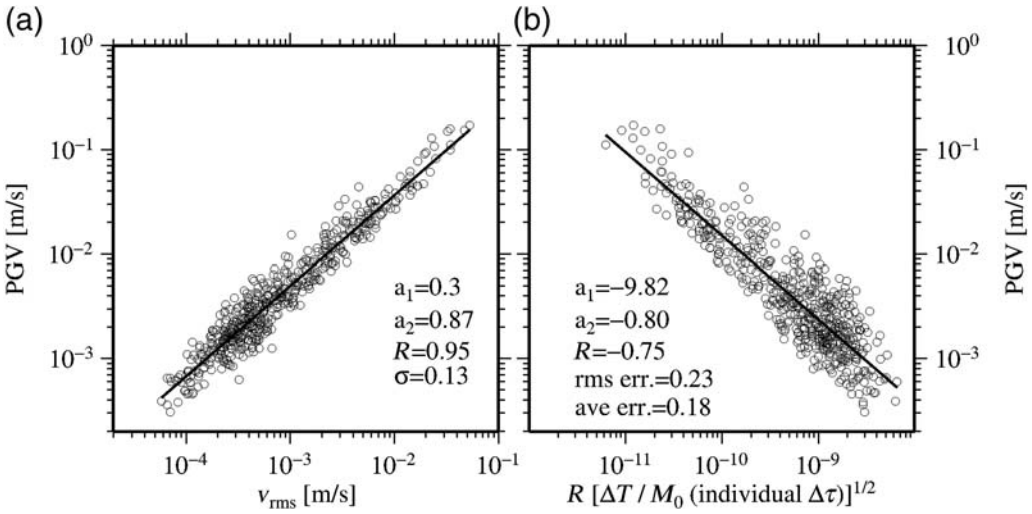

Figure 10. Empirical relations for peak ground velocities (PGVs). (a) Observed PGV as a function of observed v_{rms}, with best-fitting curve to $\log(\text{PGV}) = a_1 + a_2 \log(v_{rms})$. (b) Observed PGV as a function of calculated $R(\Delta T/\Delta\tau M_0)^{0.5}$, with best-fitting curve to $\log(\text{PGV}) = a_1 + a_2 \log[R(\Delta T/\Delta\tau M_0)^{0.5}]$. Fitting coefficients along with relevant statistical parameters are reported on each panel.

The algorithm is tested using offline KiK-borehole data from Japan. It is shown that it is possible to recover the M_w and the stress drops in real time. A couple of example timelines of seismic moment and stress drop are presented. These show that the source parameters of small-to-moderate magnitudes may be estimated quite accurately within 5 to 10 s since the first trigger, whereas those of larger magnitudes (i.e., $M_w > 6$) take 20–30 s. Finally, GMPEs for v_{rms} and PGV are presented. Once the hypocenter, the seismic moment, and the stress drop are determined using a few stations nearest to the epicenter, their values can be plugged into those equations to get the ground-motion intensity at sites further away from it.

Data and Resources

The seismograms used in this study were obtained from the KiK-net strong-motion networks accessible through http://www.kyoshin.bosai.go.jp/ (last accessed January 2016).

Acknowledgments

We thank Associate Editor Ivan Wong for his assistance. We thank Adrien Oth and an anonymous reviewer for their insightful remarks. This research was supported by Grant Number 1081/14 from the Israel Science Foundation.

References

Aki, K. (1967). Scaling law of seismic spectrum, *J. Geophys. Res.* **72,** 1217–1231.

Allmann, B. P., and P. M. Shearer (2009). Global variations of stress drop for moderate to large earthquakes, *J. Geophys. Res.* **114,** no. B01310, doi: 10.1029/2008JB005821.

Baltay, A. S., and T. C. Hanks (2014). Understanding the magnitude dependence of PGA and PGV in NGA-West 2 data, *Bull. Seismol. Soc. Am.* **104,** no. 6, 2851, doi: 10.1785/0120130283.

Böse, M., C. Ionescu, and F. Wenzel (2007). Earthquake early warning for Bucharest, Romania: Novel and revised scaling relations, *Geophys. Res. Lett.* **34,** L07302, doi: 10.1029/2007GL029396.

Brown, H. M., R. M. Allen, M. Hellweg, O. Khainovski, D. Neuhauser, and A. Souf (2011). Development of the ElarmS methodology for earthquake early warning: Realtime application in California and offline testing in Japan, *Soil Dynam. Earthq. Eng.* **31,** 188–200, doi: 10.1016/j.soildyn.2010.03.008.

Brune, J. N. (1970). Tectonic stress and the spectra of seismic shear waves from earthquakes, *J. Geophys. Res.* **75,** 4997–5009.

Caprio, M., M. Lancieri, G. B. Cua, A. Zollo, and S. Wiemer (2011). An evolutionary approach to real-time moment magnitude estimation via inversion of displacement spectra, *Geophys. Res. Lett.* **38,** L02301, doi: 10.1029/2010GL045403.

Colombelli, S., and A. Zollo (2015). Fast determination of earthquake magnitude and fault extent from real-time *P*-wave recordings, *Geophys. J. Int.* **202,** no. 2, 1158–1163, doi: 10.1093/gji/ggv217.

Cotton, F., R. Archuleta, and M. Causse (2013). What is sigma of the stress drop?, *Seismol. Res. Lett.* **84,** no. 1, 42–48, doi: 10.1785/0220120087.

Cua, G., M. Fischer, T. Heaton, and S. Wiemer (2009). Real-time performance of the virtual seismologist earthquake early warning algorithm in southern California, *Seismol. Res. Lett.* **80,** no. 5, 740–747, doi: 10.1785/gssrl.80.5.740.

Hanks, T. C. (1979). *b* values and $\omega^{-\gamma}$ seismic source models: Implications for tectonic stress variations along active fault zones and the estimation of high-frequency strong ground motion, *J. Geophys. Res.* **84,** 2235–2242.

Hanks, T. C., and H. Kanamori (1979). A moment magnitude scale, *J. Geophys. Res.* **84,** 2348–2350.

Hanks, T. C., and R. K. McGuire (1981). The character of high frequency strong ground motion, *Bull. Seismol. Soc. Am.* **71,** 2071–2095.

Hanks, T. C., and W. Thatcher (1972). A graphical representation of seismic source parameters, *J. Geophys. Res.* **23,** 4393–4405.

Küperkoch, L., T. Meier, A. Brüstle, J. Lee, and W. Friederich (2012). Automated determination of *S*-phase arrival times using autoregressive prediction: Application to local and regional distances, *Geophys. J. Int.* **188,** no. 2, 687–702, doi: 10.1111/j.1365-246X.2011.05292.x.

Kurzon, I., F. L. Vernon, A. Rosenberger, and Y. Ben-Zion (2014). Real-time automatic detectors of *P* and *S* waves using singular value decomposition, *Bull. Seismol. Soc. Am.* **104,** 13–22, doi: 10.1785/0120130295.

Lior, I., A. Ziv, and R. Madariaga (2016). *P*-wave attenuation with implications for earthquake early warning, *Bull. Seismol. Soc. Am.* **106,** 13–22, doi: 10.1785/0120150087.

Madariaga, R. (1976). Dynamics of an expanding circular fault, *Bull. Seismol. Soc. Am.* **65,** 163–182.

Oth, A. (2013). On the characteristics of earthquake stress release variations in Japan, *Earth Planet. Sci. Lett.* **377/378,** 132–141, doi: 10.1016/j.epsl.2013.06.037.

Oth, A., D. Bindi, S. Parolai, and D. Di Giacomo (2011). Spectral analysis of K-NET and KiK-net data in Japan, part II: On attenuation characteristics, source spectra, and site response of borehole and surface stations, *Bull. Seismol. Soc. Am.* **101,** no. 2, 667–687, doi: 10.1785/0120100135.

Oth, A., S. Parolai, and D. Bindi (2011). Spectral analysis of K-NET and KiK-net data in Japan, part I: Database compilation and peculiarities, *Bull. Seismol. Soc. Am.* **101,** no. 2, 652–666, doi: 10.1785/0120100134.

Ross, Z. E., and Y. Ben-Zion (2014). Automatic picking of direct *P*, *S* seismic phases and fault zone head waves, *Geophys. J. Int.* **199,** no. 1, 368–381, doi: 10.1093/gji/ggu267.

Satriano, C., L. Elia, C. Martino, M. Lancieri, A. Zollo, and G. Iannaccone (2011). PRESTo, the earthquake early warning system for southern Italy: Concepts, capabilities and future perspectives, *Soil Dynam. Earthq. Eng.* **31,** no. 2, 137–153, doi: 10.1016/j.soildyn.2010.06.008.

Wu, Y. M., and L. Zhao (2006). Magnitude estimation using the first three seconds *P*-wave amplitude in earthquake early warning, *Geophys. Res. Lett.* **33,** L16312, doi: 10.1029/2006GL026871.

Wu, Y. M., R. M. Allen, and C. F. Wu (2005). Revised M_L determination for crustal earthquakes in Taiwan, *Bull. Seismol. Soc. Am.* **95,** 2517–2524, doi: 10.1785/0120050043.

Zollo, A., G. Iannaccone, M. Lancieri, L. Cantore, V. Convertito, A. Emolo, G. Festa, F. Gallovič, M. Vassallo, C. Martino, *et al.* (2009). Earthquake early warning system in southern Italy: Methodologies and performance evaluation, *Geophys. Res. Lett.* **36,** L00B07, doi: 10.1029/2008GL036689.

Department of Geophysics
Tel-Aviv University, Ramat-Aviv
Tel-Aviv 69978, Israel
zivalon@tau.ac.il

Manuscript received 18 March 2016;
Published Online 8 November 2016